

Optimization of inflow waveform phase-difference for minimized total cavopulmonary power loss

Onur Dur¹, Curt G. DeGroff², Bradley B. Keller³, Kerem Pekkan^{1, 4}

¹Biomedical Engineering Department, Carnegie Mellon University, Pittsburgh, PA

²Congenital Heart Center, University of Florida, Gainesville, FL

³Cardiovascular Innovation Institute, University of Louisville, Louisville, KY

⁴Mechanical Engineering Department, Carnegie Mellon University, Pittsburgh, PA

Running Title: Caval waveform optimization in TCPC

Address for Correspondence:

Kerem Pekkan, PhD.

Assistant Professor – Biomedical & Mechanical (courtesy) Engineering

School of Biomedical Engineering

Carnegie Mellon University

2100 Doherty Hall, Pittsburgh, PA

Phone: (412) 268 3027

Fax: (404) 268 9807

e-mail: kpekk@andrew.cmu.edu

Abstract

The Fontan operation is a palliative surgical procedure performed on children born with congenital heart defects that have yielded only a single functioning ventricle. The Total Cavo-Pulmonary Connection (TCPC) is the most popular variant of the Fontan procedure, where the superior vena cava (SVC) and inferior vena cava (IVC) are routed directly into the pulmonary arteries (PA). Due to the limited pumping energy available optimized hemodynamics, in turn minimized power loss, inside the TCPC pathway is required for the best optimal surgical outcomes. To complement ongoing efforts to optimize the anatomical geometric design of the surgical Fontan templates, here we focused on the characterization of power loss changes due to the temporal variations in between SVC and IVC flow waveforms. An experimentally validated pulsatile computational fluid dynamics (CFD) solver is used to quantify the effect of *phase-shift* between SVC and IVC inflow waveforms and amplitudes on internal energy dissipation. The unsteady hemodynamics of two standard idealized TCPC geometries are presented incorporating patient-specific real-time PC-MRI flow waveforms of ‘functional’ Fontan patients. The effects of respiration and pulsatility on the internal energy dissipation of the TCPC pathway are analyzed. Optimization of phase-shift between caval flows is shown to lead to lower energy dissipation up to 30% in these idealized models. For physiological patient-specific caval waveforms, the power loss is reduced significantly (up to 11%) by the optimization of all three major harmonics at the same mean pathway flow (3 L/min). Thus, the hemodynamic efficiency of single-ventricle circuits is influenced strongly by the caval flow waveform quality which is regulated through respiratory dependant physiological pathways. . The proposed patient-specific waveform optimization protocol may potentially inspire new therapeutical applications to aid post-operative hemodynamics and improve the well being of the Fontan patients.

1. Introduction

Since the introduction of the Fontan procedure [1] as a palliative surgical repair for patients with various forms of complex congenital heart defects, the hemodynamics of these so-called “right heart by-pass circuits” have been studied extensively using in-vitro, in vivo, analytical, and computational techniques to achieve the ideal total cavopulmonary (TCPC) design with least energy dissipation [2]. A recent review concludes that much work still remains if we are to ever truly understand TCPC hemodynamics [3]. With the advance of CFD coupled shape optimization paradigm, automated shape design techniques [4] were recently applied to optimize the anatomical design of TCPC connections renovating the commonly employed trial-and-error based design approach [5-15].

Unsteady TCPC flow studies initially focused on flow instability under steady caval inflow conditions. Several bulk flow structures such as streamwise helical vortices, recirculation zones, cross-sectional vortex cores, and secondary flows have been found in both idealized and anatomical connection templates [8, 14-20]. Wang et al. [20] recently showed that there is an internal power loss variation of around 7% due to the inherent unsteadiness for a “functional” (i.e. healthy) patient-specific TCPC anatomy with offset. Computational studies with pulsatile physiological inflow conditions [21-23] reported higher mean TCPC power loss values than the corresponding steady inflow case at the identical pathway flow rate utilizing high resolution numerical solvers. These findings demand a detailed investigation of the physical mechanisms of *unsteady* caval waveforms that influence internal energy dissipation. Specifically, the effect of dynamic interactions between SVC and IVC inflow, which stem from the variation of magnitude and relative *phase-shift* between the vena cava waveforms, on the energy dissipation inside the TCPC has been overlooked, to our knowledge.

Detailed unsteady caval flow analysis is also crucial for the physiological understanding of univentricular circulation. In single ventricular Fontan circuits, systemic and pulmonary circulations are separated and placed in a series circuit. This configuration allows for the regulation of venous flow to occur through diaphragm movement, generating variations in intrathoracic pressure which functions as a “respiratory venous blood pump” [2]. In addition to the inspiratory augmentation of cavopulmonary blood flow, cardiac and peripheral muscular pumps [24] also affect caval flow in alternate ways depending upon the physiological condition (i.e. rest, exercise) and disease state (i.e. atrial arrhythmias, venous congestion, ventricle failure, etc). Another unique characteristic of the Fontan circulation is the negative dependence of total cardiac output (CO) (and the capacity to increase CO at exercise) on the TCPC pathway resistance i.e. sensitivity: $-0.88 \text{ L/Min per Woods Units (WU)}$ based on circuit analog single ventricle circulation models [25-27] and $-0.23 \text{ L/Min per WU}$ according to clinical data (n: 16 subjects) [27]. In contrast, negligible sensitivity was estimated for the biventricular circulation ($-0.064 \text{ L/Min per WU}$). Hence, a physiological increase in cardiac output may be possible by the improvement in TCPC flow resistance [27]. During exercise, the benefit of hydrodynamically efficient surgical pathways on CO is further augmented [28]. Likewise, the caval waveform modulation through the action of the respiratory pump and unsteady venous hemodynamics may pose a novel pathway for physiological control of the TCPC flow resistance to augment higher CO. The potential dynamic interactions between caval flows resulting from respiration, cardiac pulse or poor Fontan hemodynamics, provide the impetus for the current study. We hypothesized that temporal variations both in magnitude and phase of the caval waveforms influence the energetics inside the TCPC geometry; and, if optimized, may lead to lower viscous

dissipation. To test this hypothesis two sets of computational fluid dynamics simulations were performed:

- 1) *Analysis of relative shape of caval flow waveforms:* The effect of phase-shift and amplitude between sinusoidal SVC and IVC inlet waveforms on the energy dissipation were studied. For this analysis, two hydrodynamic performance extremes of TCPC geometry are utilized, namely one diameter offset (1DO) and zero diameter offset (0DO) standard idealized models.
- 2) *A typical patient-specific waveform optimization scenario:* Based on the results of the above analysis, the major harmonic components of a given patient-specific non-gated PC-MRI caval waveform [29] were altered and a synthetic optimum caval flow waveform having the same total CO was constructed for that patient. The energy dissipation inside the 1DO TCPC was compared for both the original and the new optimal caval waveforms.

2. Methods

2.1 Computational model and solver settings

Computational fluid dynamics (CFD) was employed to calculate the pulsatile hemodynamics inside two standard idealized planar TCPC models; the 1DO and 0DO models. In the 1DO model, the IVC was anastomosed to the right pulmonary artery (RPA) one vessel diameter away from the SVC; whereas, in the 0DO model, both caval veins (IVC and SVC) were positioned in a trivially misaligned vertical axis approximating the '+' shape conduit. A trivial misaligned caval anastomosis (~0.1 vessel diameter offset) was preferred for the 0DO TCPC since a perfect zero-offset anastomosis adds unnecessary complexity to the computational model and is surgically

unrealistic. The TCPC geometry had constant diameter ($D=1.34$ cm) tubular vessel walls, this diameter was derived from anatomic MRI data of an eight year old TCPC patient acquired by Ensley et al. [8]. Both models had flared connections with a radius of curvature of 6.7 mm at the intersection of the vena cavae and the pulmonary arteries to improve the efficiency of TCPC geometry [2, 7].

Figure 1 shows the TCPC geometry discretized with tetrahedral elements using the grid generation software, GAMBIT (ANSYS Inc., Lebanon, NH). Grid independency of the solution was ensured by comparing the solutions at five refinement levels; coarse (150,000 elements), medium (250,000 elements), fine (500,000 elements), finer (750,000 elements) and finest (1,100,000) grids. Medium grid results were presented in this study since the estimated power loss converged closely to the grid independent results with optimum computational cost and stability characteristics (Table I). For the TCPC model, the cycle-to-cycle variations reported in Table I for different grid densities are associated with the physical flow unsteadiness which can be predicted ideally with a full DNS solution. CFD models incorporated experimentally validated unsteady 2nd order accurate solver [20, 30] in FLUENT version 6.3.26 (ANSYS Inc., Lebanon, NH) to simulate incompressible and Newtonian blood flow with constant hemodynamic properties ($\rho = 1060$ kg/m³, $\mu = 3.71 \times 10^{-3}$ Pa.s). The no-slip boundary condition was enforced at the vessel walls which were assumed rigid and impermeable. Single harmonic and multi-harmonic caval waveforms are discretized into 48 and 100 time-steps respectively. Convergence was achieved by reducing the residual of the continuity equation by 10^{-6} at all time steps. The first three flow cycles were excluded from the analysis in order to ensure that the nonlinear start-up effects were eliminated. For the patient specific waveforms with complex

shape, results are reported for the sixth respiration cycle as the start-up effects were extended up to the fifth respiration cycle.

2.2 Inflow boundary conditions for waveform shape analysis

Periodic inflow conditions ($uA|_{IVC,SVC} = Q_{IVC,SVC}(t)$) were specified at the inlet boundaries of the IVC and SVC to allow for the investigation of the effect of phase-shift between the caval waveforms on power loss. For the purpose of focusing solely on single harmonic phase-shifts of caval waveforms, the inflow velocities at the IVC and SVC were represented by physiologically relevant sinusoidal functions. The complex shape of a general caval waveform was studied through its Fourier transform as presented in Section 2.2.2. In order to be compatible with the baseline flow conditions of earlier studies [8, 14] and to compare the computed power loss values, all inlet flow waveforms were scaled to provide 4L/min of mean pediatric cardiac output. The period of the each cycle was specified to be one second ($f=1$ Hz) and mean IVC to SVC flow ratio was set to 0.6/0.4 based on physiological PC-MRI data [31].

2.2.1 Implementation of respiratory effects

Respiration has been incorporated in the CFD models recently [11, 22] through a novel 2-stage method where the respiratory compensated cardiac flow component and the PC-MRI based physiological approximation of respiratory flow component are superimposed to construct the caval inflow waveforms. Although providing good qualitative agreement for the IVC flow waveform, this method discards the precise time-dependant definition of the waveforms which is required for identifying and/or modulating the inherit phase differences between the caval

waveforms. Therefore, here we incorporated non-gated simultaneous ECG, respiration and PC-MRI/Doppler Ultrasound data to simulate the respiration effects in TCPC.

Patient-specific, non-cardiac or non-respiratory gated, i.e. real-time caval flow data in patients with TCPC is limited. Analysis of the only available multi-channel acquisition of caval waveforms, respiratory and ECG signals [29, 32, 33] reveals that the venae cavae flow waveforms at rest are mainly based on two main harmonics corresponding to respiratory and cardiac effects. The inspiratory fraction (duration of inspiration relative to full flow cycle) shows small variations within different Fontan patient groups [31] and here was assumed to be 0.5. In addition, the inspiration phase was aligned with the high flow output phase (i.e. $0 - \pi$) to represent the caval flow augmentation during inspiration.

In order to incorporate the large variability observed in respiratory effects reported in the literature [29, 31, 33, 34], two sets of caval waveforms with low and high respiratory dependency (RD) were designed. The difference between inspiratory flow, Q_{ins} and expiratory flow, Q_{exp} reflects RD and can be quantified as follows [33],

$$RD = \frac{Q_{ins} - Q_{exp}}{Q_{ins} + Q_{exp}} \times 100 \quad \dots\dots\dots (1)$$

For the low respiratory dependent waveform set, 30% RD value in IVC waveform was specified based on the Doppler ultrasound and magnetic resonance measurements reported by Hsia et al. [33] and Fogel et al. [34] respectively. For the SVC flow, an identical RD was specified, having 30% fluctuation from its mean flow rate.

The motivation for a second waveform set with high RD relies on recent studies [29, 31] featuring a larger patient population, which report an inspiratory flow fraction (IFF) (the ratio of inspiratory flow to mean flow during respiratory cycle) in the IVC of 1.9 ± 0.5 (~90% RD for single harmonic waveform) [29]. Compared to the sinusoidal waveforms with 30% RD

(IFF~1.3), reproducing the respiratory effects reported in these latter data sets requires higher caval pulsatility. Hence, as a second set of simulations which were meant to represent the high RD, a sinusoidal waveform with 100% fluctuation from the mean flow rate (i.e. IFF_{IVC}~2) was used for IVC flow. For SVC, the 30% RD (IFF~1.3) value was preserved as it agreed well with the physiological IFF_{SVC}=1.0 +0.2 reported for the SVC [29].

The phase shift between caval waveforms was introduced by assigning a phase shift angle (Φ) to the IVC waveform in 15 degree increments until the IVC led the SVC by a complete flow cycle.

$$Q_{IVC}(t) = 0.6 \cdot CO \cdot (1 + (IFF_{IVC} - 1) \cdot \sin(2\pi \cdot t + \Phi_i)) \quad \dots\dots\dots (2)$$

$$Q_{SVC}(t) = 0.6 \cdot CO \cdot (1 + (IFF_{SVC} - 1) \cdot \sin(2\pi \cdot t)) \quad \dots\dots\dots (3)$$

For 1DO and 0DO TCPC configurations, the blood flow was computed for each inlet scenario where the IVC waveform led the SVC waveform by $\Phi_i = 0, 15, 30, 45 \dots 345$ degrees (Fig. 1). These cases are indicated in Table II, where a simulation summary matrix can be found.

2.2.2 Optimization of an arbitrary caval waveform (Spectral decomposition)

Hypothesizing that the minimum power loss configuration can be achieved via phase shift angle modulation, a method to construct the optimum caval waveform was proposed. First, the patient-specific flow waveform was decomposed into its major harmonic modes through Fourier transformation;

$$Q_{IVC, SVC} = A_o + \sum_{i=1}^{IVC, SVC} A_i \cdot \cos(2\pi f_i \cdot t + \Phi_i) \quad \dots\dots\dots (4)$$

where A_0 is the cycle averaged flow rate and A_i, f_i, Φ_i , are the amplitude, frequency, and phase angle of each harmonic modes respectively. Next, the phase lag between the IVC and the corresponding SVC flow was tuned to the minimum power loss configuration for each harmonic (which is geometry dependent and does not necessarily correspond to 180° , please see Discussion Section). Finally, based on the minimum power loss configuration identified by the single harmonic phase angle optimization, all harmonic components were superposed to construct the optimum caval waveform with the least power dissipation. This energy minimization approach was evaluated for the 1DO TCPC geometry where both the original patient-specific and new optimized caval waveforms were specified in CFD simulations, Table II. The original caval flow waveforms were adopted from the characteristic patient-specific PC-MRI data acquired from a functional patient with TCPC by Hjortdal et al. (2003) [29]. Detailed spectral analysis showed that the caval waveforms at rest can be accurately reconstructed using only the three main harmonics; respiratory ($f_{\text{resp}} \sim 0.3$ Hz), cardiac ($f_{\text{cardiac}} \sim 1.8$ Hz) and tertiary ($f_{\text{tertiary}} \sim 0.6$ Hz) components as shown in Figure 2. The cardiac component coincides with the systolic peak of the cardiac cycle, whereas, the tertiary component likely is the result of flow fluctuations that occur from complex effects related to compliant vessel walls, inertia of blood flow, and downstream wave reflections.

It is worth noting that we also performed stand-alone simulations in the 1DO TCPC geometry with multiple harmonics to validate that optimum phase angle is independent of number of harmonics being used. Hence, the need to perform a costly ‘multivariate’ optimization study for optimizing each relative phase angle between the multiple harmonics of an arbitrary caval waveform is eliminated.

2.3 Outlet boundary conditions

The outflow mass-split boundary condition that was introduced in our earlier study for unsteady unidirectional TCPC flows [20, 30] was further improved upon in this study to preserve mass conservation in CFD simulations with arbitrary patient-specific caval waveform topologies having backflow (Fig. 2). Briefly, an iterative user-defined subroutine, incorporating a pressure boundary condition derived from the Bernoulli equation was assigned to the pulmonary outlets. At each inner iteration, pulmonary outlet pressures were adjusted incrementally in order to satisfy the specified 50/50 baseline flow split value between left and right lung. Systematic verification tests and characterization of this new outlet boundary condition have been conducted previously [35]. In addition, by incrementally increasing the length of the pulmonary arteries, a set of auxiliary verification runs were performed where the flow profiles at different left pulmonary artery (LPA) cross sections and at the TCPC junction were recorded. At an extension of 11 vessel diameters both the fully-developed outlet velocity profiles and no influence to the internal TCPC flow field was achieved.

2.4 Towards an experimentally motivated exact power loss analysis

The power dissipated inside the connection was calculated using the control volume approach proposed by Leefe and Gentle et al. (1987) [36] for a Lagrangian fluid element. Neglecting the heat losses and rate of work done by the walls, the average power loss inside the TCPC (\dot{E}_{loss}) for one flow cycle with period, T can be calculated as given below.

$$\dot{E}_{Loss} = -\frac{1}{T} \int_0^T \int_{CS} (p + \frac{1}{2} \rho u^2) \hat{u} \cdot \hat{n} dS dt \quad \dots\dots\dots (5)$$

$$\dot{E}_{Loss} \approx \sum_{i=1}^{IVC,SVC} \overline{p_i} \cdot \overline{Q_i} - \sum_{i=1}^{PAs} \overline{p_i} \cdot \overline{Q_i} + \frac{1}{2} \rho \int_{IVC,SVC} u^3 dA - \frac{1}{2} \rho \int_{PAs} u^3 dA \quad \dots\dots\dots (6)$$

In these formulas p, u, Q, ρ, \hat{n} refer to static pressure, velocity, flow rate, density, and surface normal at the boundaries respectively. Over-score indicates the variable area-averaged at the boundary represented by subscript i. The objective was to evaluate the numerical integration with minimum simplifying assumptions and allow comparable results with the power loss reported in *in vitro* experimental studies [13, 14]. Hence the following approach is taken. The inertial term inside the integral on the right side of the power loss equation (Eq.6) was calculated exactly without employing any numerical simplification (i.e. $\overline{u^3} \neq (\overline{u})^3$) as suggested by Grigioni [37]. Implementation of this method in experimental settings, which incorporates correction coefficients on Eq. 6 replacing the detailed velocity profile information, is successfully demonstrated by the same author. The energy loss due to pressure drop was estimated using the area averaged pressure ($\overline{p_i}$) and flow rate ($\overline{Q_i}$) at the boundaries in order to comply with the limited velocity and profile available in experimental settings [13, 37]. This method provided approximately 10-15% improvement in the power loss calculation compared to the simplified control volume approach [13]. Hence results appeared closer to the power loss calculated by the velocity gradient based dissipation function [38] which is used to generate the power dissipation contour maps reported in the results section. The power loss calculation for the 1DO TCPC model was based on one converged respiratory cycle due to the periodicity of the solution (small cycle-to-cycle variations, refer to Section 3.1), whereas the ensemble running average of the power loss was reported through typically 10 converged respiratory cycles for the 0DO TCPC

model due to the inherit flow transients that were previously reported in idealized the 0DO [16] and anatomic models [19, 20].

3. Results

3.1. Effect of Caval phase-shift on power loss:

The cycle averaged power loss, in both TCPC models, changed with the caval flow phase differences, as presented in Figure 3. For the 0DO model, the power loss increased significantly to 34% at $\Phi=15^\circ$ from the baseline configuration where the waveforms are in-phase ($\Phi=0^\circ$). Power loss increased at all non-zero phase shift angles and the average increase was about 20% from the baseline for the waveforms with low respiratory dependency. Analogous to the chaotic fluctuations reported in our earlier work [20], the power loss calculated at each simulated cycle alternated around $\pm 7\%$ from the ensemble averaged power loss.

For the 1DO TCPC model, power loss varied incrementally with the phase shift angle in a more predictable manner. For the waveforms with high RD, the maximum and minimum power loss occurred when the caval waveforms were in phase ($\Phi=0^\circ, 360^\circ$) and out of phase ($\Phi=180^\circ$) respectively. Rate of energy dissipation varied consistently (following a cosine waveform) about 8% ($\pm 0.1\%$) between the extrema (Fig.3). For the waveforms with low RD, the maximum power loss variation was calculated to be 2.4% ($\pm 0.1\%$) from the minimum power loss configuration where the caval waveforms were out of phase by $\Phi=180^\circ$. It is worth noting that the error bars indicated in Figure 3 represent the random numerical errors, which originate from the cycle-to-cycle variation of the power loss due to the “physical” flow instability as introduced

earlier [20]. These calculated out to 0.1% and 7% for 1DO and 0DO TCPC models respectively. It was also shown that stability errors depend weakly on the grid resolution for the 1DO TCPC geometry (Table I). The shape of the power loss curve for the low RD case was slightly different from the high RD case, possibly due to altered flow instability characteristics and numerical errors becoming significant relative to the very small power loss changes (i.e. ~ 0.1 to 0.2%).

Finally, comparing the power loss values calculated for the 0DO and 1DO geometries with low RD waveforms, the 1DO TCPC model provided approximately 35% ($\pm 6\%$) reduction in viscous dissipation and in turn higher energy efficiency. It is worthwhile noting that the reduction seen in these modulated caval waveforms can be used in some degree as compensation in a 0DO model configuration balancing out losses from to the lack of offset.

3.2. Effect of phase-shift on 3D hemodynamics

The phase-shift in caval waveforms resulted in an alternating IVC and SVC dominant flow in the TCPC junction. A series of instantaneous power dissipation and velocity vector plots depict this phenomenon (Fig. 4). For the idealized 1DO model, the equal left and right PA perfusion, caval offset and the flared walls enabled the vena cavae flow to translate uniformly to the pulmonary arteries with relatively minor entrainment in the junction. Characteristic features of the pulsatile TCPC flow i.e. recirculation zones, helical vortex structures, secondary flows [8, 17, 20] were verified in the present study. The modest laminar regime (peak Reynolds (Re) number based on vessel area, $Re_{peak}=1400$) of the idealized 1DO model with low RD waveforms resulted in minor stagnation zones, which were located at the TCPC junction by the inferior and superior sides of the LPA and RPA branches respectively. The size of the stagnation zone at the superior RPA

wall increased when the IVC flow became more dominant (i.e. high RD waveform) where the corresponding peak Re number was calculated to be 1900.

For the 1DO TCPC, the highest energy loss region was proximal to the stagnation zone superior vessel wall of the RPA where IVC flow impinges (Fig.4, $t=0.25s$). In addition, a significant contribution to the total hydrodynamic power loss was generated from the PA recirculations zones (located in the anterior RPA and superior LPA vessel walls) due to the sudden changes in instantaneous local velocity gradients. Velocity gradients were further skewed and power dissipation increased deep in the SVC conduit as the IVC stream protrudes into the SVC lumen and collapses with the incoming SVC flow. The increased energy dissipation near the IVC vessel wall (at the peripheral sides of the lumen) is related to the increased velocity gradients near the wall due to the peak IVC flow at $t=0.25$. In contrast, the SVC jet that finds its way into the IVC during the minimum IVC flow (Fig.4, $t= 0.75s$) did not produce significant power loss increase. This phenomena continued during the IVC flow deceleration phase, creating lower power dissipation values. The equal IVC-SVC flow split time-point (Fig.4, $t= 0.93s$) yielded low power loss, confirming the previous steady state analysis [17]. Although the bulk flow structures and overall flow regime in the 1DO model were very similar for different phase angles, the instantaneous power loss history within the junction and pulmonary arteries changed with the phase angle, Φ .

The other extreme of the connection geometry is the 0DO TCPC model where disturbed flow patterns appear proximal to the anastomosis and the flow is characterized by the rapid transient fluctuations caused by the collapsing IVC and SVC jets [20]. This created an enhanced mixing of individual flow streams with higher local velocities ($Re \sim 2800$ based on vessel area) and increased the dependency of power loss to the caval phase differences. Time averaged

dissipation plots reveal that power dissipation in the axial and frontal planes (Fig. 5, Section a-a) coincided with the areas of flow stagnation at the TCPC junction. The large stagnation zone due to the caval flow collapse caused high variations in flow velocity over short stream distances which increased the overall pressure drop and enhanced the viscous dissipation particularly at its downstream confluence. Therefore, the $\Phi = 345^\circ$ waveform configuration having a relatively larger stagnant zone created higher power dissipation values in the axial and frontal planes than the $\Phi = 120^\circ$ configuration, which is a typical low power loss case. The maximum power loss occurred at the locus of caval flow impingement (where the maximum pressure increase observed) which was closer to the SVC due to the higher mean flow energy of the IVC stream. In contrast, the power dissipation in the sagittal midplane (Fig.5, Section b-b) correlated with the vorticity of the secondary flows which was lower for the $\Phi = 120^\circ$ waveform compared to $\Phi = 345^\circ$. For both models, venae cavae flow became fully-developed proximal to the junction with significant pulsatility (Womersley number ~ 9). Comparing Figures 5 and 6, the time averaged bulk flow structures within the mixing zone were notably altered in 0DO TCPC geometry by the variation of the phase-angle. In contrast, for the 1DO TCPC, minor entrainment of caval flows at the junction created relatively less dependency to caval phase-differences. Therefore, the geometry dependant caval flow hemodynamics at mixing zone explains the rapid and stable power loss variation, as shown in Figure 3, in 0DO and 1DO TCPC geometries respectively.

3.3 Multi-harmonic patient-specific waveform optimization

For the “functional” patient-specific waveform, optimum waveforms were constructed for each major harmonics based on the minimum power loss configuration (i.e. $\Phi=180^\circ$ for 1DO model) identified in Section 3.1. Each IVC flow harmonic was shifted in time with respect to its corresponding SVC harmonic where both the original and optimal caval waveforms were represented with three main harmonic modes. The power loss evaluated inside the 1DO TCPC geometry incorporating the original and the optimal caval waveforms yielded significant differences; 8.43mW and 7.53mW respectively (Table III). The power dissipation was attenuated by about 11% using the optimum IVC flow waveform for this standard patient-specific waveform for the fixed surgical design. A detailed comparison of the time averaged flow structures (Fig.6) indicates that the vorticity of the secondary flows were significantly reduced in the optimized waveform configuration. Hence, the power loss reduction by the waveform optimization is associated with a decrease in the rotational strength of the counter-rotating vortices along the branch PAs.

4. Discussion

4.1 Implications of caval phase-shift on univentricular venous physiology

This study demonstrates that, in addition to the optimal baffle geometry, optimal inlet flow waveforms lead to lower TCPC power losses, which in turn augment higher CO in single ventricle circulation [27]. In normal biventricular physiology, negative intrathoracic pressure

during inspiration enhances both caval flows identically and in-phase since both venae cavae essentially terminate at the right atrium [39, 40]. In contrast, for univentricular TCPC circulation, although both caval veins are surgically anastomosed to pulmonary arteries and thus exposed to the common downstream atrium and extramural thoracic pressure, the altered impedance characteristics of the IVC baffle compared to the SVC pathway may enable caval phase shifts. In addition, the increase in abdominal pressure produced by the descent of the diaphragm during inspiration enhances mainly the IVC flow based on the relationship between downstream thoracic IVC pressure and abdominal pressure [41-43]. Comprehensive studies showed that an increase in IVC flow was higher in patients with TCPC than in normal subjects due to the hepatic venous flow stream which constitute 40% of the IVC flow and occurs primarily during the inspiration phase in TCPC patients [31, 33]. IVC flow data acquired by Hjortdal et al. [29] also confirms this observation as two flow peaks of the biphasic IVC waveform are apparent during inspiration possibly due to the aforementioned high hepatic flow and portal vein flow mismatch. Therefore, respiratory effects of intrathoracic pressure [44], unbalanced venous characteristics, abdominal pressure variation with diaphragm decent [45] and the filling function of the common atrium may cause phase differences in caval waveform harmonics. Our analysis based on the patient-specific PC-MRI data set [29] revealed finite phase differences between three major caval waveform harmonics. Expanding the current very limited, real-time (i.e. non-gated) Fontan flow data will enable further investigation on venous flow waveforms and the underlying univentricular physiology.

The contemporary final stage of the Fontan procedure often incorporates a certain degree of a caval offset which varies from 0DO to 1DO due to patient-specific major anatomical constraints and the surgical template (intra atrial vs. extra cardiac) [16, 43]. Analysis performed

on both surgical design extremes identified the phase shift angle sensitivity of the TCPC geometry for the entire offset range. The increase in power loss due to caval phase-angle variation ranged from 2.5% to 35% for 1DO and 0DO TCPC anatomies, respectively, at the same mean cardiac output of 4 L/min. Power loss inside the 1DO TCPC geometry changed with small increments consistently as the phase difference between caval waveforms changed. Whereas, 0DO geometry exhibited high sensitivity and excessive variation in power loss even for a slight alteration of IVC phase angle with respect to the SVC. In addition to lowering the power loss [14], 1DO TCPC geometry exhibits superior pulsatile behavior over the 0DO by attenuating the inflow phase angle sensitivity which is shown in this study to be critical for sustaining minimum energy loss states.

Injury of the phrenic nerve during Fontan procedures is a severe and not uncommon problem which results in diaphragm paralysis and is clinically associated with poor hemodynamic conditions [33, 46, 47], such as those seen in patients with a “failing” Fontan [48-50]. Despite surgical placcation palliation, the respiratory pump function remains suboptimal with reduced inspiratory flow augmentation and increased cavopulmonary pressure [47]. Furthermore, any possibility for active control of the caval waveform shape, particularly the phase-shift of the respiration mediated main harmonic mode, is also lost. This factor potentially contributes to the low cardiac output state by the elevated energy losses inside the TCPC associated with arbitrary caval pulsations. Therefore, in addition to the low inspiratory flow augmentation and trans-hepatic gradient [47] the perturbed energetics inside the TCPC may also be responsible for inadequate Fontan circulation and influence the progress of arterial desaturation, chronic ascites and plural effusions which are too often seen in patients with phrenic nerve palsy [46].

If clinically deemed to be beneficial the caval waveform modulation can be explored using a pulsatile bench-top pediatric single ventricle flow loop incorporating various pediatric ventricular assist devices (PVADs) anastomosed to venous return [51]. Preliminary *in vitro* experience with single-ventricle circuits suggested that phase-shifts between caval waveforms can be controlled using a continuous discharge PVAD or through external pulsation [Ahmet's poster].. The clinical applicability of these approaches are speculative and their assessment of relative risk to benefit ratio require further investigations. Emerging mechanical assist therapies for single-ventricle patients [52, 53] should consider the influence of caval flow waveform quality on the local TCPC hemodynamics.

4.3 Generalized pulsatile power loss with multiple inlets and outlets

Dasi et al. (2008) [54] recently introduced non-dimensional metrics to characterize the TCPC power dissipation with steady caval inflow and highlighted the total caval flow rate (equivalent to the CO for balanced pulmonary and systemic flows) as a major parameter determining the power loss [14, 54]. Expanding these studies, the present pulsatile investigation illustrated that for a fixed time-average physiological total caval flow rate, the mean energy loss can be altered significantly as the phase-angle between caval flows changes. Detailed investigation on TCPC flow structures suggests that the variation of the power loss by the phase-shift relates strongly to the hemodynamic response within the TCPC junction and pulmonary arteries which depend nonlinearly on the total incoming CO ($Q_{IVC} + Q_{SVC}$) and the fraction of the CO directed to each lung. Since the instantaneous total *operating* cardiac output $CO(t) = Q_{IVC}(t) + Q_{SVC}(t)$ varies significantly with the phase difference, the corresponding mean power loss is also expected to vary within these regions. Our results indicated that these instantaneous flow fluctuations are minimized when the

caval waveforms are out-of-phase which corresponds to the minimum power loss configuration for 1DO TCPC geometry. However, the unintuitive power loss increase for all non-zero phase angles draws attention to the geometry dependant nonlinear hemodynamic response within the TCPC junction. Along these lines, new clinical metrics based on the mean caval flow pulsatility and Fontan anatomic geometry [55] will likely further complement the steady TCPC power dissipation formulation [54] and can provide analytical expressions to predict pulsatile power loss changes. We expect to present these new metrics in future communications.

4.4 Final remarks and limitations

Our study highlights the need to define the precise relationship between energy losses in TCPC vessel architecture and pulsatility of unsteady flow physiologic caval flows. The proposed waveform optimization method proved to be successful by improving the energetics (i.e. 11%) in 1DO TCPC models with arbitrary patient-specific caval waveforms. To validate the congruency of the single frequency phase shift analysis with the multi-harmonic analysis, additional phase-shift analysis with cardiac frequency of 1.8 Hz is performed. The maximum power loss variation between in-phase and out-of-phase caval waveforms are computed to be 7.63% for 1.8 Hz vs. 8.63% for the 1Hz waveforms. Likewise, the effect of retrograde flow on power loss, unbalanced PA flow splits, the presence of multiple harmonics with high fluctuations and their cross-talk require additional investigation. The waveform optimization paradigm requires further *in vitro* validation and simulations incorporating different patient-specific surgical templates before it can be utilized clinically or in device designs. The rigid walled computational model has well

acknowledged limitations caused by wall elasticity and respiration dependant peripheral impedance [56, 57]. It has been shown that wall elasticity causes ~10% variation in power losses when compared to rigid models [58, 59] . Likewise, the relative impact of wall motion on power loss is probably lower than that of geometrical accuracy [60] and may have similar influence on both models. It is worth to note that due to mismatching compliances of IVC and SVC walls the accurate identification of the optimal caval phase shift will require incorporation of wall elastance. Effect of caval phase shift on power dissipation within compliant anatomical models requires further investigation. These problems should be addressed individually in future numerical studies. While the fully developed Womersley flow pattern achieved in all simulations confirmed the validity of the improved outlet boundary conditions, future models would benefit from more realistic representation of the downstream vasculature incorporating impedance based analog models [61]. Such boundary conditions, once combined with elastic wall TCPC models (requiring graft as well as diseased venous and diseased arterial vessel wall material properties), will then be able to accurately simulate flow oscillations and accurately incorporate the wave reflections from the circulation downstream to the TCPC circuit as additional harmonics. Lastly, limited real-time patient-specific data needs to be expanded upon through additional clinical studies for improved understanding of these relationships.

5. Conclusion

Exploiting the geometry dependant effect of caval waveform phase-shift on TCPC power loss, the present comparative study illustrates that for a fixed surgical design and CO, the power dissipation depends strongly on the shape of inlet vena cavae waveforms. Notable improvements

in power loss may suggest the utilization of this knowledge for the emerging therapeutical applications to aid post-operative Fontan hemodynamics. .

Acknowledgements

We acknowledge Pittsburgh Supercomputing Center grant CCR080013 facilitating the high-performance parallel CFD runs presented in this manuscript.

LIST OF TABLES

Table I: Grid sensitivity analysis for 1DO TCPC geometry incorporating in-phase single harmonic caval flow waveforms with high respiratory dependency. Percent difference indicates the difference of power loss calculated by each grid with respect to the coarse grid estimation. CPU hours are reported based on the simulations performed on eight parallel Itanium2 Montvale 9130M dual-core processors with 8.0 GB RAM shared memory. % *C-to-C* refers to the flow instability dependant cycle-to-cycle variation of power loss inside the 1DO TCPC from the average power loss calculated using running average method.

Table II: Matrix of all CFD simulations (excluding the verification runs) included in this study. 1DO: One diameter offset, 0DO: Zero diameter offset, IVC: Inferior vena cava, SVC: Superior vena cava, IFF: Inspiratory flow fraction (ratio of inspiratory flow to mean flow), RD: percent respiratory dependency. *For single-harmonic phase-shift analysis SVC flow waveform is fixed with 30% RD for all cases [29].

Table III: Power loss inside the 1DO TCPC geometry incorporating functional and optimized patient-specific caval waveforms. Phase-shift optimization is performed using the spectral waveforms with only the three main harmonics (i.e. respiratory, cardiac and tertiary flow components).

LIST OF FIGURES

Figure 1: Idealized one-diameter offset (1DO) TCPC model, diameter = 13.4 mm [left] and single harmonic of the pulsatile inlet flow waveforms for superior vena cava (SVC) and inferior vena cava with high (IVC_{HRD}) and low (IVC_{LRD}) respiratory dependency [right]. Insert shows the close-up of medium density tetrahedral mesh used in CFD simulations. Dashed lines indicate the control volume for power loss calculations. The phase shift between IVC and SVC flow waveform is increased with 15° increments by altering the IVC phase shift angle, $\Phi = 0, 15, 30, 45 \dots 345^\circ$ relative to SVC. For clarity only $\Phi = 0^\circ, 60^\circ$ (dash) and 180° (dotted) are plotted. RPA: Right pulmonary artery, LPA: Left pulmonary artery, SVC: Superior vena cava, IVC: Inferior vena cava

Figure 2: Representation of a typical patient-specific “functional” caval flow waveform [29] by its three fundamental harmonic components [left]. The full spectral decomposition of these waveforms is also provided on the right.

Figure 3: Power loss changes as a function of phase-shift angle between the sinusoidal caval waveforms for 1DO TCPC models having high [top], low [middle] respiratory dependency (RD) and 0DO TCPC model with low respiratory dependency [bottom]. Error bars indicate the cyclic variation of the power loss from the converged running ensemble averages calculated at each phase shift angle. For reference, the power loss calculated in a transient simulation with the non-pulsatile steady waveforms is also plotted.

Figure 4: Contour plots of rate of energy dissipation (E_{diss}), flow rate, pressure for zero caval phase difference ($\Phi=0^\circ$, highest power loss caval waveform pair) at different time points over the flow cycle. Based on the high respiratory dependant waveforms incorporated, IVC/SVC flow

split is time dependent and labeled at each time point, on the left. Note that the time-averaged flow split is fixed to 60/40.

Figure 5: Time averaged rate of energy dissipation (E_{diss}) and velocity vectors for two selected phase shift values; $\Phi=345^\circ$ [top] and $\Phi=120^\circ$ [bottom] leading to high and low power loss configurations respectively. Time averaged pressure contours and vorticity indicate the source of the power dissipation within the given cross section. Each subfigure at the frontal plane (+ shaped TCPC) corresponds to a rectangle with $2.5D \times 2D$ dimensions (width x height, D : vessel diameter = 1.33cm).

Figure 6: Time averaged dissipation contours (E_{diss}) for the original [top] and optimized patient specific caval waveforms [bottom]. Cross-section views display the rate of energy dissipation and vorticity magnitude.

Table I: Grid sensitivity analysis for 1D0 TCPC geometry incorporating in-phase single harmonic caval flow waveforms with high respiratory dependency. % difference indicates the difference of power loss calculated by each grid with respect to the coarse grid estimation. CPU hours are reported based on the simulations performed on eight parallel Itanium2 Montvale 9130M dual-core processors with 8.0 GB RAM shared memory. % *C-to-C* refers to the flow instability dependant cycle-to-cycle variation of power loss inside the 1D0 TCPC from the average power loss calculated using running average method.

Grid Resolution	Element count	CPU hours	Power Loss (mW)	% Difference	% CtoC Variation
Coarse	150,000	32	9.60	-	0.10
Medium	250,000	96	10.12	5.4	0.10
Fine	500,000	240	10.50	9.4	0.15
Finer	750,000	312	10.57	10.1	0.15
Finest	1,100,000	336	10.62	10.6	0.14

Table II: Matrix of all CFD simulations (excluding the verification runs) included in this study. 1DO: One diameter offset, 0DO: Zero diameter offset, IVC: Inferior vena cava, SVC: Superior vena cava, IFF: Inspiratory flow fraction (ratio of inspiratory flow to mean flow), RD: percent respiratory dependency. *For single-harmonic phase-shift analysis SVC flow waveform is fixed with 30% RD for all cases [29].

Analysis	Geometry	Inlet Waveform Topology		IVC Phase Angle (Number of simulations)
		Amplitude (IFF)	Frequency (Hz)	
Phase Shift (single harmonic)	1DO	2 (High RD)	1	0-360 (24)
		1.3 (Low RD)	1	0-360 (24)
	0DO	1.3 (Low RD)	1	0-360 (24)
Power Loss Optimization	1DO	Patient-specific functional Fontan [29] represented with 3 harmonics (IFF =1.9)	$f_{\text{resp}}, f_{\text{cardiac}}, f_{\text{tertiary}}$ 0.3, 0.6, 1.8	46, 253, 84 (1)
		Optimized 'Healthy' Fontan with 3 (modified) harmonics		All harmonics shifted 180 (Optimized waveform) (1)

Table III: Power loss inside the 1DO TCPC geometry incorporating functional and optimized patient-specific caval waveforms. Phase-shift optimization is performed using the spectral

waveforms with only the three main harmonics (i.e. respiratory, cardiac and tertiary flow components).

Analysis	Caval Waveforms	Power Loss (mW)	% Difference
Power Loss Optimization	Patient-specific functional Fontan [29] represented with 3 harmonics	8.43	-
	Optimized 'Healthy' Fontan with 3 (modified) harmonics	7.53	- 11

Figure 1: Idealized one-diameter offset (1DO) TCPC model, diameter = 13.4 mm [left] and single harmonic of the pulsatile inlet flow waveforms for superior vena cava (SVC) and inferior vena cava with high (IVC_{HRD}) and low (IVC_{LRD}) respiratory dependency [right]. Insert shows the close-up of medium density tetrahedral mesh used in CFD simulations. Dashed lines indicate the control volume for power loss calculations. The phase shift between IVC and SVC flow waveform is increased with 15° increments by altering the IVC phase shift angle, $\Phi = 0, 15, 30, 45 \dots 345^\circ$ relative to SVC. For clarity only $\Phi = 0^\circ, 60^\circ$ (dash) and 180° (dotted) are plotted. RPA: Right pulmonary artery, LPA: Left pulmonary artery, SVC: Superior vena cava, IVC: Inferior vena cava

Figure 2: Representation of a typical patient-specific “functional” caval flow waveform [29] by its three fundamental harmonic components [left]. The full spectral decompositions of these waveforms are also provided on the right.

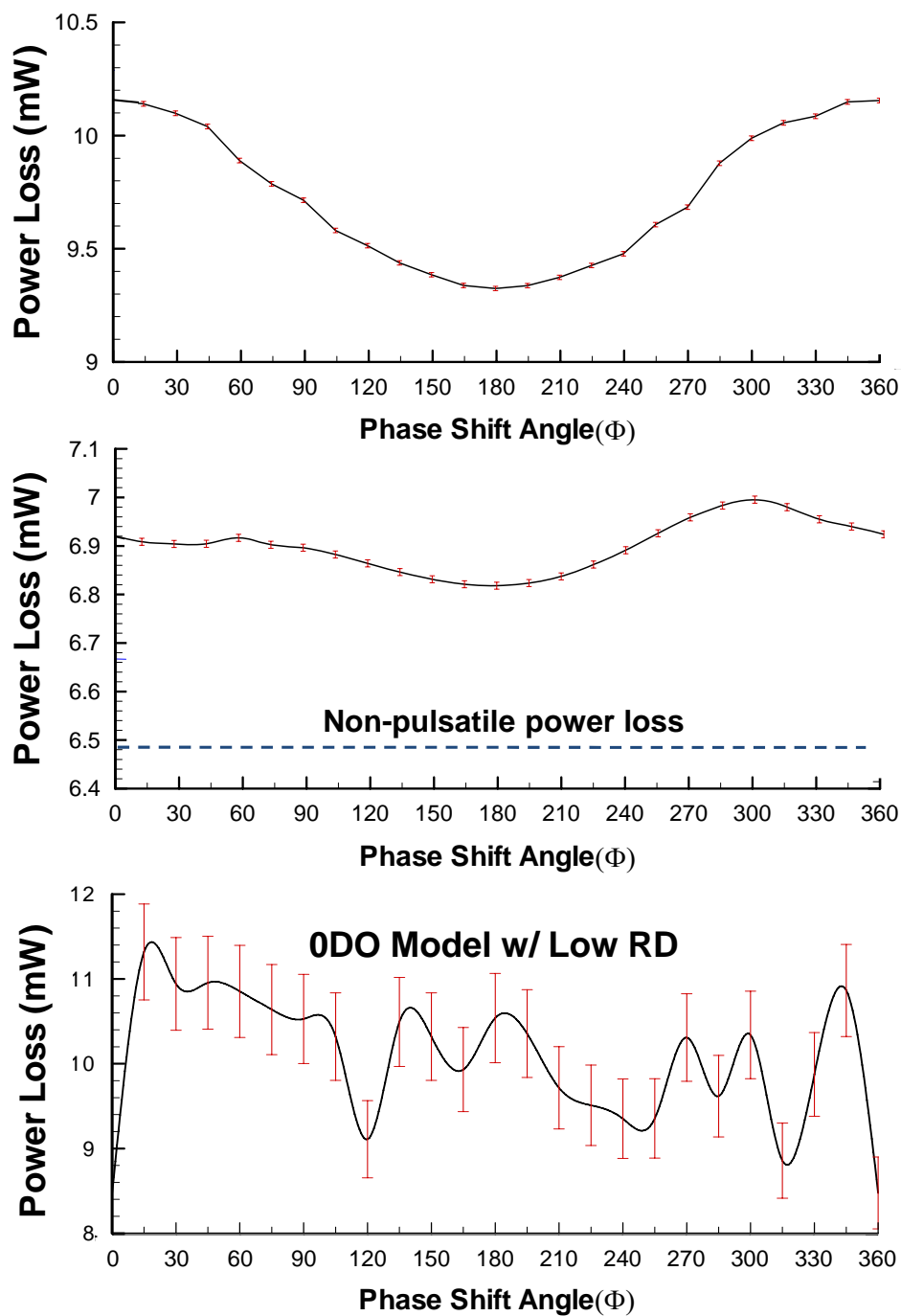


Figure 3: Power loss changes as a function of phase-shift angle between the sinusoidal caval waveforms for 1DO TCPC models having high [top], low [middle] respiratory dependency (RD) and 0DO TCPC model with low respiratory dependency [bottom]. Error bars indicate the cyclic variation of the power loss from the converged running ensemble averages calculated at each phase shift angle. For reference, the power loss calculated in a transient simulation with the non-pulsatile steady waveforms is also plotted.

Figure 4: Contour plots of rate of energy dissipation (E_{diss}), flow rate, pressure for zero caval phase difference ($\Phi=0^\circ$, highest power loss caval waveform pair) at different time points over the flow cycle. Based on the high respiratory dependant waveforms incorporated, IVC/SVC flow split is time dependent and labeled at each time point, on the left. Note that the time-averaged flow split is fixed to 60/40.

Figure 5: Time averaged rate of energy dissipation (E_{diss}) and velocity vectors for two selected phase shift values; $\Phi=345^\circ$ and $\Phi=120^\circ$ leading to high [top] and low [bottom] power loss configurations respectively. Time averaged pressure contours and vorticity indicate the source of the power dissipation within the given cross section. Each subfigure at the frontal plane (+ shaped TCPC) corresponds to a rectangle with $2.5D \times 2D$ dimensions (width x height, D : vessel diameter = 1.33cm).

Figure 6: Time averaged dissipation (E_{diss}) contours for the original [top] and optimized patient specific caval waveforms [bottom]. Cross-section views display the rate of energy dissipation and vorticity magnitude.

REFERENCES

1. Fontan F, Baudet E. Surgical repair of tricuspid atresia. Thorax. 1971;26:240-8.

2. de Leval MR, Kilner P, Gewillig M, Bull C. Total cavopulmonary connection: a logical alternative to atriopulmonary connection for complex Fontan operations. Experimental studies and early clinical experience. *J Thorac Cardiovasc Surg.* 1988;96:682-95.
3. DeGroff CG. Modeling the Fontan circulation: where we are and where we need to go. *Pediatr Cardiol.* 2008;29:3-12.
4. Weiguang Yang, Jeffrey Feinstein, V. Mohan Reddy, Marsden A. Optimization of an idealized Y-Shaped Extracardiac Fontan Baffle. 61st Annual Meeting of the APS Division of Fluid Dynamics; 2008; San Antonio, Texas; 2008.
5. Bove EL, de Leval MR, Migliavacca F, Guadagni G, Dubini G. Computational fluid dynamics in the evaluation of hemodynamic performance of cavopulmonary connections after the Norwood procedure for hypoplastic left heart syndrome. *J Thorac Cardiovasc Surg.* 2003;126:1040-7.
6. de Leval MR, Dubini G, Migliavacca F, Jalali H, Camporini G, Redington A, et al. Use of computational fluid dynamics in the design of surgical procedures: application to the study of competitive flows in cavo-pulmonary connections. *J Thorac Cardiovasc Surg.* 1996;111:502-13.
7. Ensley AE, Lynch P, Chatzimavroudis GP, Lucas C, Sharma S, Yoganathan AP. Toward designing the optimal total cavopulmonary connection: an in vitro study. *Ann Thorac Surg.* 1999;68:1384-90.
8. Ensley AE, Ramuzat A, Healy TM, Chatzimavroudis GP, Lucas C, Sharma S, et al. Fluid mechanic assessment of the total cavopulmonary connection using magnetic resonance phase velocity mapping and digital particle image velocimetry. *Ann Biomed Eng.* 2000;28:1172-83.
9. Gerdes A, Kunze J, Pfister G, Sievers HH. Addition of a small curvature reduces power losses across total cavopulmonary connections. *Ann Thorac Surg.* 1999;67:1760-4.
10. Kim YH, Walker PG, Fontaine AA, Panchal S, Ensley AE, Oshinski J, et al. Hemodynamics of the Fontan connection: an in-vitro study. *J Biomech Eng.* 1995;117:423-8.
11. Marsden AL, Bernstein AJ, Reddy VM, Shadden SC, Spilker RL, Chan FP, et al. Evaluation of a novel Y-shaped extracardiac Fontan baffle using computational fluid dynamics. *J Thorac Cardiovasc Surg.* 2009;137:394-403 e2.
12. Migliavacca F, de Leval MR, Dubini G, Pietrabissa R, Fumero R. Computational fluid dynamic simulations of cavopulmonary connections with an extracardiac lateral conduit. *Med Eng Phys.* 1999;21:187-93.
13. Ryu K, Healy TM, Ensley AE, Sharma S, Lucas C, Yoganathan AP. Importance of accurate geometry in the study of the total cavopulmonary connection: computational simulations and in vitro experiments. *Ann Biomed Eng.* 2001;29:844-53.
14. Sharma S, Goudy S, Walker P, Panchal S, Ensley A, Kanter K, et al. In vitro flow experiments for determination of optimal geometry of total cavopulmonary connection for surgical repair of children with functional single ventricle. *J Am Coll Cardiol.* 1996;27:1264-9.
15. Soerensen DD, Pekkan K, de Zelicourt D, Sharma S, Kanter K, Fogel M, et al. Introduction of a new optimized total cavopulmonary connection. *Ann Thorac Surg.* 2007;83:2182-90.
16. DeGroff C, Birnbaum B, Shandas R, Orlando W, Hertzberg J. Computational simulations of the total cavo-pulmonary connection: insights in optimizing numerical solutions. *Med Eng Phys.* 2005;27:135-46.
17. Khunatorn Y, Mahalingam S, DeGroff CG, Shandas R. Influence of connection geometry and SVC-IVC flow rate ratio on flow structures within the total cavopulmonary connection: a numerical study. *J Biomech Eng.* 2002;124:364-77.

18. Migliavacca F, de Leval MR, Dubini G, Pietrabissa R. A computational pulsatile model of the bidirectional cavopulmonary anastomosis: the influence of pulmonary forward flow. *J Biomech Eng.* 1996;118:520-8.
19. Pekkan K, de Zelicourt D, Ge L, Sotiropoulos F, Frakes D, Fogel MA, et al. Physics-driven CFD modeling of complex anatomical cardiovascular flows-a TCPC case study. *Ann Biomed Eng.* 2005;33:284-300.
20. Wang C, Pekkan K, de Zelicourt D, Horner M, Parihar A, Kulkarni A, et al. Progress in the CFD modeling of flow instabilities in anatomical total cavopulmonary connections. *Ann Biomed Eng.* 2007;35:1840-56.
21. DeGroff GC, Shandas R. Designing the optimal Total Cavopulmonary Connection: pulsatile versus steady flow experiments. *Med Sci Monit.* 2002;8:41-5.
22. Marsden AL, Vignon-Clementel IE, Chan FP, Feinstein JA, Taylor CA. Effects of exercise and respiration on hemodynamic efficiency in CFD simulations of the total cavopulmonary connection. *Ann Biomed Eng.* 2007;35:250-63.
23. Migliavacca F, Dubini G, Bove EL, de Leval MR. Computational fluid dynamics simulations in realistic 3-D geometries of the total cavopulmonary anastomosis: the influence of the inferior caval anastomosis. *J Biomech Eng.* 2003;125:805-13.
24. Rowland TW. The circulatory response to exercise: role of the peripheral pump. *Int J Sports Med.* 2001;22:558-65.
25. Pekkan K, Frakes D, De Zelicourt D, Lucas CW, Parks WJ, Yoganathan AP. Coupling pediatric ventricle assist devices to the Fontan circulation: simulations with a lumped-parameter model. *ASAIO J.* 2005;51:618-28.
26. Sundareswaran K, Pekkan K, Zelicourt d, D. D, L. P. K, H. W, et al. Significant impact of the total cavopulmonary connection (TCPC) resistance on cardiac output and exercise performance in single ventricles. The American Heart Association (AHA) Scientific Sessions 2007; Orange County Convention Center - Orlando, FL; 2007.
27. Sundareswaran KS, Pekkan K, Dasi LP, Whitehead K, Sharma S, Kanter KR, et al. The total cavopulmonary connection resistance: a significant impact on single ventricle hemodynamics at rest and exercise. *Am J Physiol Heart Circ Physiol.* 2008;295:H2427-35.
28. Whitehead KK, Pekkan K, Kitajima HD, Paridon SM, Yoganathan AP, Fogel MA. Nonlinear power loss during exercise in single-ventricle patients after the Fontan: insights from computational fluid dynamics. *Circulation.* 2007;116:I165-71.
29. Hjortdal VE, Emmertsen K, Stenbog E, Frund T, Schmidt MR, Kromann O, et al. Effects of exercise and respiration on blood flow in total cavopulmonary connection: a real-time magnetic resonance flow study. *Circulation.* 2003;108:1227-31.
30. Pekkan K, Dur O, Sundareswaran K, Kanter K, Fogel M, Yoganathan A, et al. Neonatal aortic arch hemodynamics and perfusion during cardiopulmonary bypass. *J Biomech Eng.* 2008;130:061012.
31. Hjortdal VE, Christensen TD, Larsen SH, Emmertsen K, Pedersen EM. Caval blood flow during supine exercise in normal and Fontan patients. *Ann Thorac Surg.* 2008;85:599-603.
32. Houliind K, Stenbog EV, Sorensen KE, Emmertsen K, Hansen OK, Rybro L, et al. Pulmonary and caval flow dynamics after total cavopulmonary connection. *Heart.* 1999;81:67-72.
33. Hsia TY, Khambadkone S, Redington AN, Migliavacca F, Deanfield JE, de Leval MR. Effects of respiration and gravity on infradiaphragmatic venous flow in normal and Fontan patients. *Circulation.* 2000;102:III148-53.

34. Fogel MA, Weinberg PM, Hoydu A, Hubbard A, Rychik J, Jacobs M, et al. The nature of flow in the systemic venous pathway measured by magnetic resonance blood tagging in patients having the Fontan operation. *J Thorac Cardiovasc Surg.* 1997;114:1032-41.
35. Dur O, DeGroff GC, Pekkan K. Effect of caval flow waveform on the energy dissipation of failing Fontan patients *Journal of Biomechanical Engineering.* 2009;manuscript in preperation.
36. Leefe SE, Gentle CR. Theoretical evaluation of energy loss methods in the analysis of prosthetic heart valves. *J Biomed Eng.* 1987;9:121-7.
37. Grigioni M, D'Avenio G, Amodeo A, Di Donato RM. Power dissipation associated with surgical operations' hemodynamics: critical issues and application to the total cavopulmonary connection. *J Biomech.* 2006;39:1583-94.
38. Healy TM, Lucas C, Yoganathan AP. Noninvasive fluid dynamic power loss assessments for total cavopulmonary connections using the viscous dissipation function: a feasibility study. *J Biomech Eng.* 2001;123:317-24.
39. Guyton AC, Coleman TG, Granger HJ. Circulation: overall regulation. *Annu Rev Physiol.* 1972;34:13-46.
40. Takata M, Beloucif S, Shimada M, Robotham JL. Superior and inferior vena caval flows during respiration: pathogenesis of Kussmaul's sign. *Am J Physiol.* 1992;262:H763-70.
41. Robotham JL, Takata M. Mechanical abdomino/heart/lung interaction. *J Sleep Res.* 1995;4:50-2.
42. Takata M, Robotham JL. Effects of inspiratory diaphragmatic descent on inferior vena caval venous return. *J Appl Physiol.* 1992;72:597-607.
43. Takata M, Wise RA, Robotham JL. Effects of abdominal pressure on venous return: abdominal vascular zone conditions. *J Appl Physiol.* 1990;69:1961-72.
44. Penny DJ, Redington AN. Doppler echocardiographic evaluation of pulmonary blood flow after the Fontan operation: the role of the lungs. *Br Heart J.* 1991;66:372-4.
45. Decramer M, De Troyer A, Kelly S, Zocchi L, Macklem PT. Regional differences in abdominal pressure swings in dogs. *J Appl Physiol.* 1984;57:1682-7.
46. Amin Z, McElhinney DB, Strawn JK, Kugler JD, Duncan KF, Reddy VM, et al. Hemidiaphragmatic paralysis increases postoperative morbidity after a modified Fontan operation. *J Thorac Cardiovasc Surg.* 2001;122:856-62.
47. Hsia TY, Khambadkone S, Bradley SM, de Leval MR. Subdiaphragmatic venous hemodynamics in patients with biventricular and Fontan circulation after diaphragm plication. *J Thorac Cardiovasc Surg.* 2007;134:1397-405; discussion 405.
48. Anderson PA, Sleeper LA, Mahony L, Colan SD, Atz AM, Breitbart RE, et al. Contemporary outcomes after the Fontan procedure: a Pediatric Heart Network multicenter study. *J Am Coll Cardiol.* 2008;52:85-98.
49. Ghanayem NS, Berger S, Tweddell JS. Medical management of the failing Fontan. *Pediatr Cardiol.* 2007;28:465-71.
50. Marino BS. Outcomes after the Fontan procedure. *Curr Opin Pediatr.* 2002;14:620-6.
51. Dur O, Lara M, Arnold D, Vandenbergh S, Keller B, DeGroff C, et al. Pulsatile in vitro simulation of the pediatric univentricular circulation for evaluation of cardiopulmonary assist scenarios. *Artif Organs.* 2009;in review.
52. Pekkan K, Sasmazel A, Sundareswaran K, Parks WJ, Kanter K, Lucas C, et al. Respiratory Augmentation of Blood Flow in the Early Post-Op Fontan Circulation – Feasibility of Intra-Pulmonic Balloon Pumping and External Counterpulsation of Systemic Venous Return. *16th World Congress of the World Society of Cardio-Thoracic Surgeons.* Ottawa, Canada 2006.

53. Throckmorton AL, Ballman KK, Myers CD, Frankel SH, Brown JW, Rodefeld MD. Performance of a 3-bladed propeller pump to provide cavopulmonary assist in the failing Fontan circulation. *Ann Thorac Surg.* 2008;86:1343-7.
54. Dasi LP, Pekkan K, Katajima HD, Yoganathan AP. Functional analysis of Fontan energy dissipation. *J Biomech.* 2008;41:2246-52.
55. KrishnankuttyRema R, Dasi LP, Pekkan K, Sundareswaran K, Fogel M, Sharma S, et al. Quantitative analysis of extracardiac versus intraatrial Fontan anatomic geometries. *Ann Thorac Surg.* 2008;85:810-7.
56. Ketner MW, Lucas CL, Mill MR, Sheridan B, Lucas W. Energetics and hemodynamic changes of normal and various right heart bypass (Fontan) circulations in lambs under varying respiration parameters. *Conf Proc IEEE Eng Med Biol Soc.* 2004;5:3785-8.
57. Lucas C, Ketner M, Steele B, Mill M.R, Sheridan B, Lucas W.J, et al. Importance of respiration and graft compliance in Fontan circulations: Experimental and computational studies. *Journal of Biomechanics.* 2006;39:S207.
58. Orlando W, Shandas R, DeGroff C. Efficiency differences in computational simulations of the total cavo-pulmonary circulation with and without compliant vessel walls. *Comput Methods Programs Biomed.* 2006;81:220-7.
59. Masters JC, Ketner M, Bleiweis MS, Mill M, Yoganathan A, Lucas CL. The effect of incorporating vessel compliance in a computational model of blood flow in a total cavopulmonary connection (TCPC) with caval centerline offset. *J Biomech Eng.* 2004;126:709-13.
60. Jin S, Oshinski J, Giddens DP. Effects of wall motion and compliance on flow patterns in the ascending aorta. *J Biomech Eng.* 2003;125:347-54.
61. Vignon-Clementel I, Figueroa A, Jansen K, C T. Outflow boundary conditions for three-dimensional finite element modeling of blood flow and pressure in arteries. *Comput Methods Appl Mech Eng.* 2006;195:3776-96.